

Nematic Ordering of Suspensions of Charged Anisotropic Colloids Detected by ^{23}Na Nuclear Magnetic Resonance

P. Porion,[†] M. Al Mukhtar,[†] S. Meyer,[†] A. M. Faugère,[†] J. R. C. van der Maarel,[‡] and A. Delville^{*,†}

CRMD, CNRS, 1B rue de la Férollerie, 45071 Orléans Cedex 02, France and Soft Condensed Matter Group, Leiden Institute of Chemistry, Leiden University, Leiden, The Netherlands

Received: February 7, 2001; In Final Form: June 27, 2001

A detailed line shape analysis of ^{23}Na nuclear magnetic resonance spectra within dense suspensions (12% vol/vol) of Laponite clay exhibits a macroscopic ordering of these charged anisotropic colloids within a nematic phase. The angular variation of the order parameter limits to 20% of the maximum amount of disorder in these dense suspensions. By contrast, dilute Laponite suspensions (1–4% vol/vol) remain isotropic while the variation of ^{23}Na relaxation rates over a broad range of frequencies indicates a local ordering of the clay platelets within microdomains of the same spatial extent than the particle diameter (300 Å).

I. Introduction

Charged colloids display a large variety of physicochemical properties (swelling, adhesion, sol/gel transition, thixotropy, ionic exchange, adsorption) used in numerous industrial applications (civil engineering, food, paints or cosmetics industry, water treatment, waste management). When the concentration of suspensions of charged spherical colloids increases, they display a sequence of gas/liquid- and liquid/solid-like transitions, generally well described by equations of state based on renormalized volume fraction^{1,2} used to describe the overlaps between the clouds of counterions surrounding each colloid. Suspensions of charged anisotropic colloids were recently the subject of numerous studies^{3–12} since their mechanical behavior is more complex than that of spherical colloids, because of the competition between electrostatic^{4,13} and excluded volume effects.^{14–16} As an example, energetic contributions, driven by electrostatic forces, were shown to orient neighboring charged disks perpendicular to each other^{4,13} while entropic contributions,^{14–16} driven by excluded volume effects, are optimized by parallel alignment of the same neighboring disks. As liquid crystals,^{17–22} suspensions of anisotropic charged colloids^{23–31} are also able to form locally ordered tactoids or even nematic phases, depending on the shape and the aspect ratio of the charged colloids.

Clay particles are ubiquitous materials, constituting a large class of charged anisotropic colloids, involved in numerous industrial applications. For this study, we used Laponite RD, a synthetic hectorite, because of its high purity and well characterized chemical composition. It is composed of one octahedral layer of magnesium oxides sandwiched between two tetrahedral layers of silicon oxides. Some Mg(II) atoms of the octahedral layer are replaced by Li(I) atoms, resulting in a negative charge on the particle neutralized by exchangeable sodium counterions. The general formula of Laponite is $(\text{OH})_4\text{Si}_8\text{Mg}_{5.33}\text{Li}_{0.67}\text{O}_{20}\cdot\text{Na}_{0.67}$. Laponite clay particles are easily dispersed in water and behave as isolated disks (diameter 300–400 Å, thickness 10

Å), each neutralized by exchangeable sodium counterions. Although Laponite aqueous suspensions were the subject of numerous recent studies,^{3–12} the origin of their organization¹¹ and mechanical behavior⁴ is not well understood. As an example, dilute Laponite suspensions display a microsegregation at low ionic strength¹¹ and a liquid/gas-like first-order transition at higher salt concentration.⁴ Both observations require some effective attraction between the clay particles, while these clay dispersions are purely repulsive.^{4,8,11} The equation of state of the Laponite suspensions at high salt concentration exhibits a plateau over a broad range of clay concentrations⁴ that cannot be interpreted as resulting from an Onsager isotropic/nematic transition^{14–16} but requires the occurrence of some effective interparticle attraction as for the liquid/gas transition. Furthermore, no macroscopic phase separation^{4,11} was detected during this first-order transition, and no direct evidence of macroscopic ordering was reported from nuclear magnetic resonance^{32,33} or cryofracture^{4,11} experiments.

We have used ^{23}Na nuclear magnetic resonance to gain information on the local structure and the dynamical behavior of the Laponite particles through inspection of the nuclear relaxation behavior of their strongly bound neutralizing counterions.^{32–33} Quadrupolar counterions, initially condensed at the surface of a clay particle, are sensitive to the orientation of this particle because it determines the magnitude of their quadrupolar coupling.³² Since Laponite diffusion and reorientation occur at a time scale ($> 1 \mu\text{s}$)^{10,12} many orders of magnitude larger than the time scale corresponding to the motion of the small ions, the dynamical simulations of the decorrelation of the quadrupolar coupling may be performed assuming immobile clay particles. Monte Carlo simulations of sodium hydration at the clay/water interface exhibit a residual static component of the electrostatic field gradient³² felt by the sodium counterions condensed on the clay surface. Since this residual field gradient is linked to the clay particle with its principal axis perpendicular to the clay surface,³² ionic diffusion is the only mechanism allowing condensed counterions to lose the memory of their quadrupolar coupling by successive adsorption on clay particles with *different* orientations. Fast local motions, such as ion desorption, obviously induce high-frequency fluctuations of the

* Corresponding author. E-mail: delville@cnrs-orleans.fr

[†] CRMD, CNRS.

[‡] Leiden University.

total quadrupolar coupling, but they are unable to lose the memory of the residual quadrupolar coupling of initially condensed counterions as long as their adsorption occurs later on a clay particle parallel to the initial one. As a consequence, the frequency variation of the quadrupolar relaxation rates of the ^{23}Na and ^7Li nuclei in dilute clay suspensions (1–4% vol/vol) are driven by ionic diffusion through the porous network constituted by the clay particles.^{32–33} The frequency variation of the relaxation rates suggests local ordering of the clay particles within microdomains of the same size as the particle diameter.^{32–33} ^{23}Na nuclear magnetic resonance of dense suspensions of Laponite (12% vol/vol) gives direct evidence of nematic ordering by the detection of a residual static coupling. As for liquid crystals, this static coupling is the fingerprint of a macroscopic ordering obtained by increasing the concentration of initially isotropic suspensions.

II. Materials and Methods

Laponite RD was purchased from Laporte and used without treatment. Diluted clay suspensions (between 1 and 4% vol/vol) were dispersed by stirring during 1 h in pure water 10^{-2} M salt (NaCl) at pH 10 (obtained by adding NaOH) to prevent dissolution of the Laponite particles.³⁴ Dense samples were prepared by oedometric uniaxial compression at 3 atm during 2 weeks. We used ultrafiltration membranes (Osmonics Inc.) with pore size $0.1\ \mu\text{m}$ to reduce the loss of the small Laponite clay particles (diameter $300\ \text{\AA}$, thickness $10\ \text{\AA}$). In order not to alter the organization of the clay particles, two small cylinders (diameter 8 mm) were directly cut in the whole filtration cake (thickness 2 mm) and carefully introduced in the NMR tube. By this way, the macroscopic direction of the compression applied to the clay sample remains parallel to the longitudinal axis of the NMR tube. The final density of the compressed sample (12% vol/vol) was determined by gravimetry after water loss at $80\ ^\circ\text{C}$ under vacuum. Montmorillonite (Wyoming) sample was purified according to standard procedure.³⁵

^{23}Na NMR spectra were recorded on Bruker spectrometers (DSX 360, MSL 200, DSX 100) with a static field of 8.465, 4.702, and 2.351 T, respectively. T_1 measurements were performed using the classical inversion–recovery pulse sequence, and T_2 measurements by the Hahn spin–echoes procedure. Spectra were recorded on the DSX spectrometers with a broad spectral width (1 MHz) and a fast acquisition procedure. Relaxation measurements at low fields ($\omega = 10^5$ – $10^6\ \text{s}^{-1}$) were obtained from spin-locking $T_{1\rho}$ experiments.

Details on the quadrupolar relaxation of spin-3/2 nuclei under residual static coupling and radio frequency pulses are given in the Appendix. From the numerical integration of equations A12–15 and A17–20, we are able to calculate the time evolution of the different coherences during each elementary step (RF pulse, delay, acquisition, Fourier transform) of the different NMR experiments (single pulse, T_1 , T_2 and $T_{1\rho}$ measurements). We used a Simplex fitting procedure³⁶ to determine the various parameters (ω_Q , $J(0)$, $J(\lambda_1)$, $J(\lambda_2)$, $J(\omega_0)$ and $J(2\omega_0)$) by minimizing the mean squared deviation between the set of experimental and simulated data. As an example, Figure 7 exhibits the agreement obtained for the line shape analysis and Figures 8a–b for the $T_{1\rho}$ experiments. The set of parameters results from a simultaneous fit of the different NMR experiments (T_1 , T_2 , $T_{1\rho}$ and line shape analysis). The information on the spectral density are collected in Figure 9, and the angular variation of the residual quadrupolar splitting (ω_Q) is displayed in Figure 10.

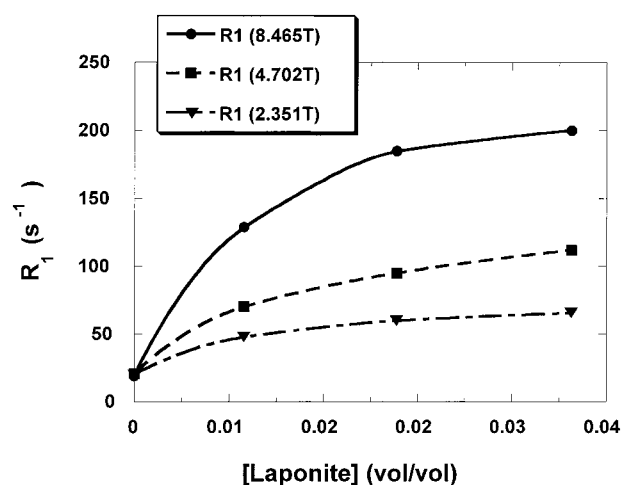


Figure 1. Frequency variation of the longitudinal relaxation rate of ^{23}Na in dilute suspensions of Laponite clay.

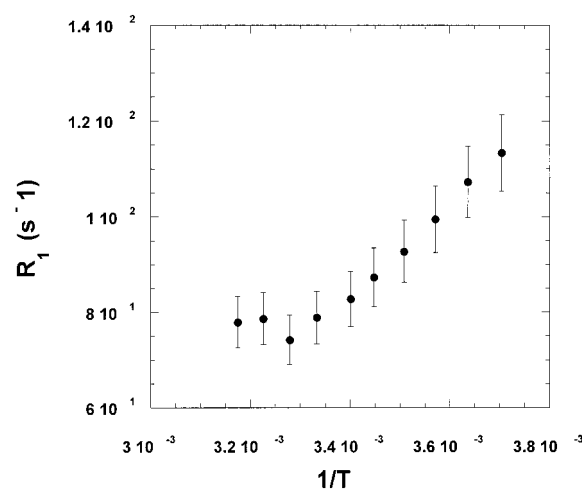


Figure 2. Temperature variation of the longitudinal relaxation rate of ^{23}Na in a suspension of Laponite clay.

III. Results

A. Low-Density Isotropic Suspensions. To investigate the potential of nuclear magnetic resonance, we first studied dilute suspensions of Laponite clays (concentration $\leq 4\%$ vol/vol). The frequency variation of the relaxation rates of Figure 1 is the fingerprint of a slow modulation of the quadrupolar coupling felt by sodium counterions in the vicinity of the clay particle. The temperature variation displayed in Figure 2 is in agreement with a fast exchange (at the NMR time scale) of sodium cations free in the solution and those condensed in the electrostatic well in the vicinity of the clay particles. That fraction of condensed counterions is responsible for the large enhancement of the ^{23}Na relaxation rates in the presence of clay. Note that the temperature variation of the longitudinal relaxation rate totally precludes the interpretation of the data displayed in Figure 1, i.e., the frequency variation of the longitudinal relaxation rates, by a classical BPP model,⁵⁰ assuming an exponential decorrelation of the quadrupolar Hamiltonian with a single correlation time.

Since no quadrupolar splitting of the ^{23}Na resonance line was detected, these dilute clay suspensions appear isotropic in the orientation of the clay platelets with respect to the field. The results displayed in Figure 3 suggest two frequency regimes: a power law at high frequency and a plateau at low frequency. Unfortunately, a large gap remains between the frequency domains covered by the sets of T_1 and $T_{1\rho}$ experiments. To

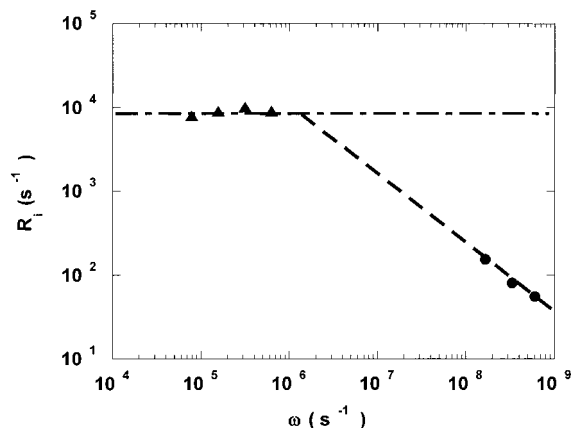


Figure 3. Frequency variation of the relaxation rates ($1/T_1$ and $1/T_{1\rho}$) of ^{23}Na nuclei in a dilute Laponite suspension. The dashed lines are drawn to better visualize the two frequency regimes discussed in the text.

interpret these data, we performed a multiscale modeling of ion diffusion within heterogeneous clay dispersions.^{32–33} The starting point of this analysis was a molecular modeling of the clay/water interface,³⁷ showing a nonvanishing residual value of the electric field gradient (efg) felt by the sodium counterions condensed in contact with the clay surface ($V_{zz} = (7 \pm 3) 10^{19}$ SI units).³² This efg is evaluated by grand canonical Monte Carlo simulations of the hydration shell (thickness 30 Å) pertaining to one fragment of the clay particle neutralized by 14 sodium counterions.³² This calculation of the efg experienced by each sodium counterion includes the contributions from the atomic electric charges of the clay particle, the electric charges of the other sodium counterions and the dipolar contribution from the cation hydration shell, which is distorted by the solid/liquid interface.³² Because of the high anisotropy of this clay hydration layer, the principal axis of the efg tensor is perpendicular to the clay surface. Note that this derivation a priori overestimates the effective value of the residual splitting since not every sodium counterion is necessarily localized within a 30 Å shell centered on the clay particle. As an example, previous Monte Carlo simulations of ionic condensation around Laponite clay particles with a separation of 100 Å have shown that only 50% of the total amount of counterions are effectively localized within such shell.⁴⁷

Since clay reorientation occurs at a time scale ($> \mu\text{s}$)^{10,12} much larger than the time scale accessible by NMR ($\tau \sim 1/\omega_0 \sim 10$ ns), we suggested a relaxation mechanism implying ionic diffusion.^{32–33} In a first-order approximation, we neglect the small contribution of free sodium. An initially condensed sodium counterion will recover a large part of its initial quadrupolar coupling by diffusing freely through the suspension and hitting another clay particle with nearly the same orientation as its initial clay particle. The spectral density was then calculated as the Fourier transform of the autocorrelation function characterizing the loss of memory of the residual quadrupolar Hamiltonian during the free diffusion of a single sodium cation within the clay network:

$$G_Q(\tau) = \frac{15 \langle V_{zz} \rangle^2 N_{\text{at}} N_{\text{pt}} N_{\text{pt}}}{32 N_{\text{at}} \pi} \sum_{i=1}^{N_{\text{at}}} \sum_{j=1}^{N_{\text{pt}}} \sum_{k=1}^{N_{\text{pt}}} p(i \in j|0) p(i \in k|\tau) \times (3\cos^2 \theta_j - 1)(3\cos^2 \theta_k - 1) \quad (1)$$

where N_{at} and N_{pt} are, respectively, the total number of sodium cations and clay particles, $p(i \in k|\tau)$ is the probability of finding

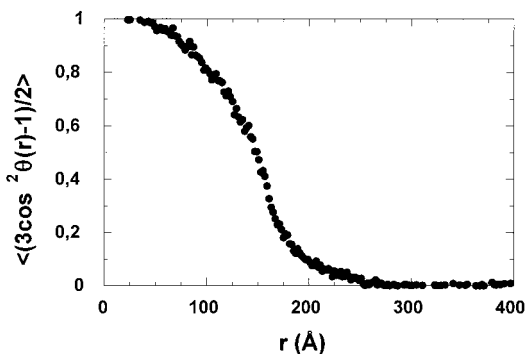


Figure 4. Local ordering within dilute suspension of hard disks (diameter 300 Å, thickness 10 Å).

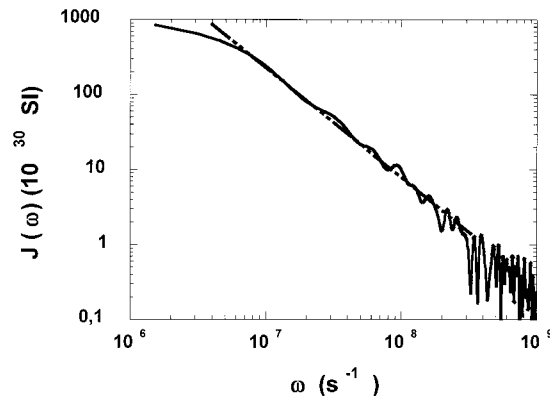


Figure 5. Numerical simulations of the spectral density calculated for diffusion of sodium cation within diluted clay suspensions.

ion i condensed on the clay particle k at time τ and θ_j is the angle between the normal to the surface of the clay particle j and the static magnetic field.

The frequency variation of the spectral density (Figure 3) is thus the consequence of the propagation of local orientation ordering of the clay particles in the suspension. By Monte Carlo simulations of the organization of hard disks (diameter 300 Å, thickness 10 Å) in the same dilute regime, we obtained ordering of the suspensions within micro-domains of size of the disk diameter (Figure 4). The frequency variation of the spectral density was then reproduced (Figure 5) by simple Brownian dynamics of a single sodium probe, without any interaction except for an average residence time of 1 ns on the clay surface.^{32–33} We detected the same dynamical regimes as those displayed in Figure 3. However, the agreement is only semi-quantitative since the slope predicted by the Brownian simulations ($J(\omega) \approx \omega^{-1.5 \pm 0.5}$) differs somewhat from the experimental value ($J(\omega) \approx \omega^{-0.9 \pm 0.1}$). This discrepancy is not surprising because of the simplicity of our model. We considered only the coexistence between two limiting environments and focused on the long time evolution of the autocorrelation function of the quadrupolar coupling by neglecting any local and fast motions that may contribute significantly to the spectral density in the high-frequency domain. Further simulations of molecular dynamics are now under progress to improve this approach by taking into account the influence of the long-range electric field generated by the charge of the clay particle and its neutralizing counterions on the trajectories of the collectively diffusing sodium cations.

The frequency crossover between the low-frequency plateau and the high-frequency power law displayed by the spectral densities (Figures 3 and 5) is related to the spatial extent of the microdomains constituted from nearly parallel clay particles

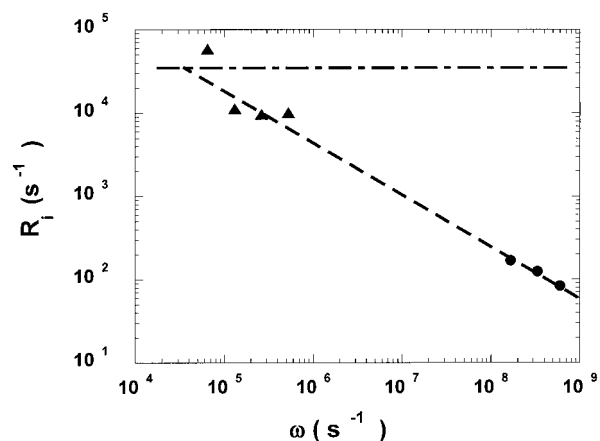


Figure 6. Frequency variation of the relaxation rates ($1/T_1$ and $1/T_{1\rho}$) of ^{23}Na nuclei in a dilute Montmorillonite suspension.

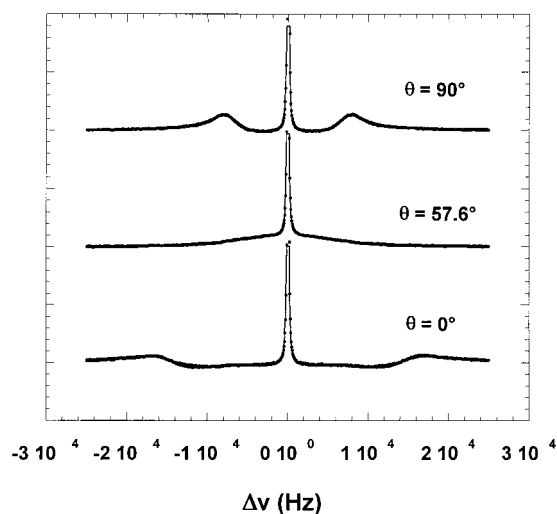


Figure 7. Comparison the line shape recorded by ^{23}Na NMR in a dense Laponite suspension (●) and result from theoretical simulations (continuous curve).

(Figure 4): 100 ns is the time required for sodium cation ($D \sim 10^{-5} \text{ cm}^2/\text{s}$) to travel across a domain of size 100 Å. Replacing the small Laponite particle (diameter 300 Å) by larger Montmorillonite clay (persistence length ~ 3000 Å)³⁸ shifts the crossover frequency to lower values by two decades (Figure 6) since the ordered microdomains are larger by 1 order of magnitude.

Of course, the frequency domains investigated here are somewhat limited, assuredly restricting the applicability of the method. Nevertheless, the spectral density is sampled in this study over three complementary ranges of angular velocities: first, at zero angular velocity, by the T_2 measurements; second, within the range $\omega_1 \in [10^5, 10^6] \text{ s}^{-1}$, by the $T_{1\rho}$ experiments; and third, within the range $\omega_0 \in [10^8, 10^9] \text{ s}^{-1}$, by the T_1 experiments.

Relaxation measurement with a field cycling spectrometer is certainly a powerful procedure to fill the gap between these frequency domains, but it may be useless in our case because of the fast relaxation of the magnetization and the time necessary to switch the magnetic field.

B. High-Density Nematic Suspension. Contrasting with the spectra recorded for dilute clay suspensions, the spectra observed for concentrated Laponite suspensions prepared by uniaxial compression display a large residual quadrupolar splitting (ω_Q

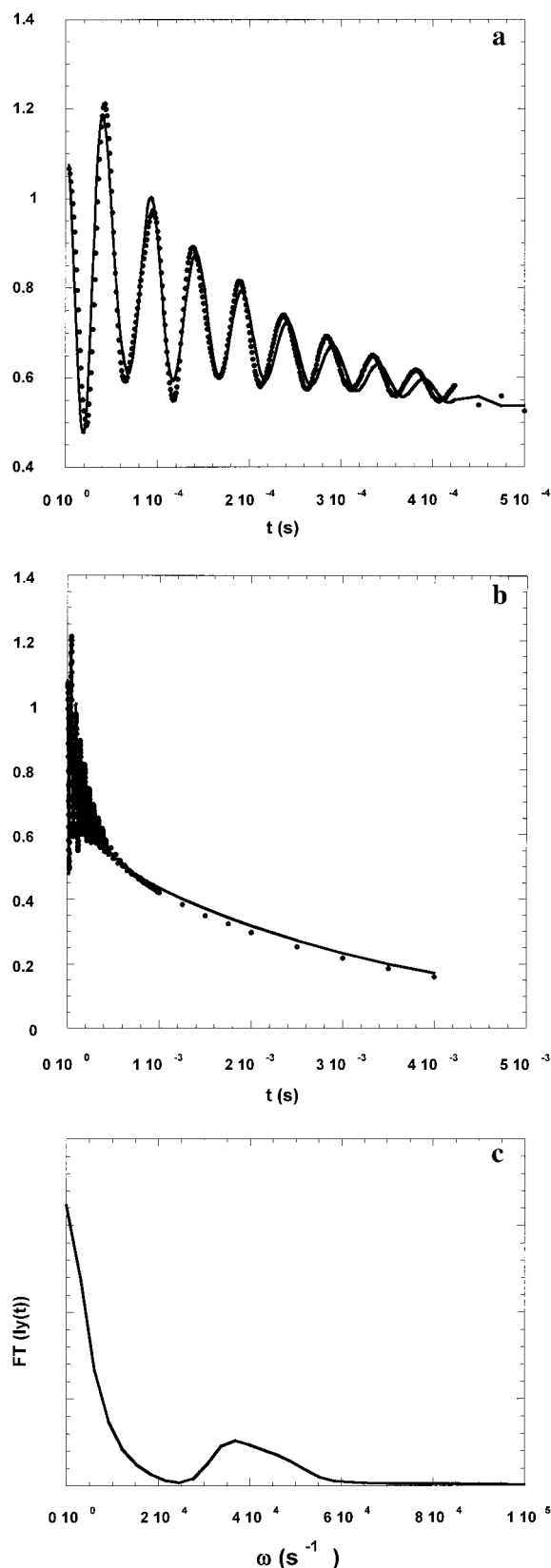


Figure 8. Time variation (a and b) and its Fourier transform (c) of the transverse magnetization under spin locking experiment performed by ^{23}Na NMR in a dense Laponite suspension.

$\sim 9 \times 10^4 \text{ s}^{-1}$) which varies as a function of the orientation in the static magnetic field of the NMR tube (or the direction of the compression axis of the sample) (Figure 7). This result confirms our prediction (see above) of a residual nonvanishing

TABLE 1: Coefficients Defining the $m = 0$ Contribution of the Relaxation Term (cf eqs A14–15 and eqs A19–20)^a

	$J_0(\lambda_1)$	$J_0(\lambda_2)$	$J_0(0)$
A	$\omega_1(\omega_Q + \omega_1)/\lambda_1^2$	$\omega_1(\omega_Q - \omega_1)/\lambda_2^2$	$-2\omega_1\omega_Q(\omega_Q^2 + 2\omega_1^2)/\lambda_1^2\lambda_2^2$
B	$-\omega_1(\omega_Q + \omega_1)/\lambda_1^2$	$\omega_1(\omega_Q - \omega_1)/\lambda_2^2$	$-2\omega_1^2(\omega_Q^2 - 4\omega_1^2)/\lambda_1^2\lambda_2^2$
C	$-\omega_1(\omega_Q - 2\omega_1)/\lambda_1^2$	$\omega_1(\omega_Q + 2\omega_1)/\lambda_2^2$	$2(\omega_Q^4 + 8\omega_1^4)/\lambda_1^2\lambda_2^2$
D	$\omega_1(\omega_Q + 4\omega_1)/\lambda_1^2$	$-\omega_1(\omega_Q - 4\omega_1)/\lambda_2^2$	$2\omega_Q^2(\omega_Q^2 + 2\omega_1^2)/\lambda_1^2\lambda_2^2$
E	$\omega_1(\omega_Q + 4\omega_1)/\lambda_1^2$	$\omega_1(\omega_Q - 4\omega_1)/\lambda_2^2$	$-2\omega_1\omega_Q(\omega_Q^2 - 4\omega_1^2)/\lambda_1^2\lambda_2^2$
F	$-\omega_1^2/\lambda_1^2$	ω_1^2/λ_2^2	$-4\omega_1^3\omega_Q/\lambda_1^2\lambda_2^2$
G	ω_1^2/λ_1^2	ω_1^2/λ_2^2	$2/3[\omega_Q^4 + \omega_Q^2\omega_1^2 + 4\omega_1^4]/\lambda_1^2\lambda_2^2$
H	$\omega_1(\omega_Q + 3\omega_1)/\lambda_1^2$	$-\omega_1(\omega_Q - 3\omega_1)/\lambda_2^2$	$2/3[2\omega_Q^4 + 5\omega_Q^2\omega_1^2 - 4\omega_1^4]/\lambda_1^2\lambda_2^2$
I	$-\omega_1(\omega_Q - \omega_1)/\lambda_1^2$	$\omega_1(\omega_Q + \omega_1)/\lambda_2^2$	$2/3[2\omega_Q^4 - \omega_Q^2\omega_1^2 + 20\omega_1^4]/\lambda_1^2\lambda_2^2$
J	$\omega_1(\omega_Q - \omega_1)/\lambda_1^2$	$\omega_1(\omega_Q + \omega_1)/\lambda_2^2$	$-2\omega_1\omega_Q(\omega_Q^2 + 6\omega_1^2)/\lambda_1^2\lambda_2^2$

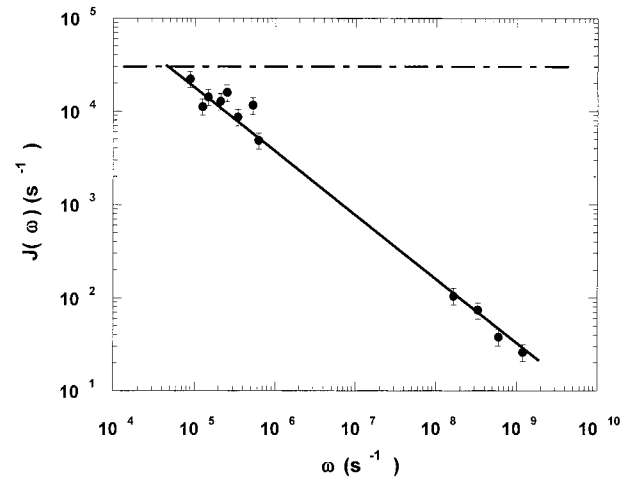
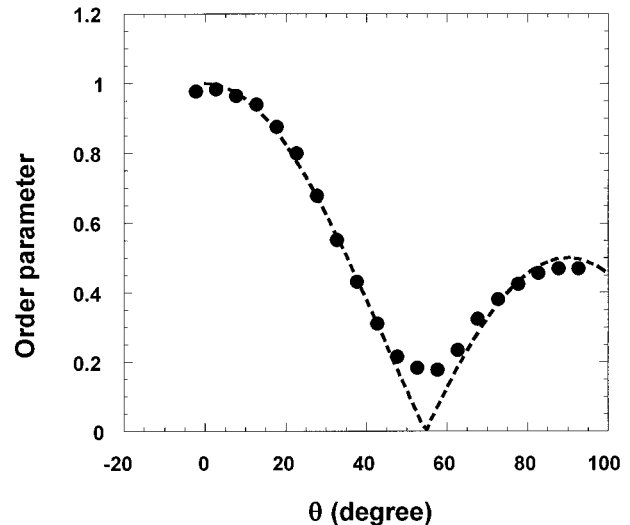
$$^a \lambda_1 = \sqrt{\omega_Q^2 + 2\omega_1\omega_Q + 4\omega_1^2} \text{ and } \lambda_2 = \sqrt{\omega_Q^2 - 2\omega_1\omega_Q + 4\omega_1^2}$$

value of the electric field gradient felt by the sodium counterions condensed in the vicinity of the clay particles.³² The residual quadrupolar splitting calculated by our molecular model of the clay/water interface³² ($V_{zz} = 7 \times 10^{19}$ SI) is four times larger than the measured value. That discrepancy is not surprising, since not all sodium counterions are condensed at the clay surface. As discussed in section IIIA, we estimate to 50% the amount of sodium counterions localized near to the clay surface (at separation less than 15 Å) and contributing to the static field gradient. The detected residual splitting^{39,40} (Figure 7) is the consequence of a nematic ordering of the whole clay sample. The largest splitting is observed when the direction of the compression axis is parallel to the magnetic field, as expected for alignment of the particle directors parallel to this compression axis. The two satellites of the triplet, which represent 60% of the detected magnetization, are broader than the central line since they relax faster than this central component because of the slow modulation of the quadrupolar coupling.⁴¹

The analysis of the line shapes detected in Figure 7 requires a detailed description of the time evolution of the different coherences of the spin-3/2 nuclei under RF pulse and slow modulation of their quadrupolar coupling.⁴² In particular, it was necessary to take into account the influence of the coherence relaxation even during a single RF pulse, because it mixes the one quantum coherences of all ranks (T_{11} , T_{21} , and T_{31}), inducing a depletion of the baseline near the central resonance peak of the triplet. Note that near the magic angle, the residual splitting cancels out and the line shape then becomes equivalent to that recorded for isotropic dilute suspensions.

The procedure used to simulate the line shape shown on Figure 7 is described in the Appendix. This analysis requires the knowledge of the spectral density. Preliminary relaxation measurements (T_1 , T_2 , and $T_{1\rho}$) are thus performed in order to extract this information. The details are also given in the Appendix. Figures 8a,b give a typical illustration of these $T_{1\rho}$ experiments. As detailed in Table 1, the time evolution of the fast component of the transverse magnetization ($I_y \propto T_{11}(s)$) during a $T_{1\rho}$ experiment results from the interference between three contributions with time constants defined as linear combination of the spectral densities $J_0(0)$, $J_0(\lambda_1)$, and $J_0(\lambda_2)$. A Fourier transform analysis of the time variation of the magnetization exhibits a dominant contribution centered at zero angular frequency and a secondary asymmetrical contribution covering a broad range of angular velocities ($\omega \in [25000 \text{ s}^{-1}, 55000 \text{ s}^{-1}]$). To avoid spurious oscillations resulting from the long-time cutoff of the transverse magnetization, data from Figure 8a,b are apodized prior to Fourier transform. This apodization reduces the contribution from the slow relaxation rates and broadens the power spectrum by 5000 s^{-1} . The Simplex fitting procedure³⁶ (see Appendix) is useful to extract the value of the spectral density (Figure 9) over a broad range

of frequencies. The error analysis of the generalized last squared deviation implied in our fitting procedure gives a maximum accuracy of about 30% on the low-frequency values of the spectral density. Here, also we detect a crossover between two dynamical regimes: a plateau at low frequency and a power law at high frequency. By contrast with the conclusions obtained for isotropic diluted samples, this crossover frequency ($\sim 5 \times 10^4 \text{ s}^{-1}$) now gives information on the time scale (and thus spatial extent) of the microdomains over which sodium cation must diffuse in order to record fluctuations of the average directors of the clay particles. These relaxation measurements

**Figure 9.** Frequency variation of the spectral density of ^{23}Na nuclei in dense Laponite suspension.**Figure 10.** Variation of the order parameter detected by ^{23}Na NMR in a dense nematic Laponite suspension.

were performed for clay samples with the macroscopic director oriented perpendicular to the static field. While the $T_{1\rho}$ relaxation times are sensitive to the sample orientation⁴³ through the value of the residual splitting (cf data from Table 1 and the Appendix), we have checked that neither the longitudinal and transverse relaxation times nor the spectral density were sensitive to the sample orientation in the static field.

Finally, by using the spectral density from Figure 9, it was possible to analyze the line shape (see Appendix) measured for different orientations of the NMR tube in the static field, sampled between 0° and 90° by steps of 5°. Experimental and fitted spectra are plotted in Figure 8 for some orientations of the sample, illustrating the perfect agreement between our theoretical treatment of the time evolution of the coherences and the experimental data. The residual static coupling was obtained by the Simplex fitting procedure (see Appendix) and normalized with respect to its maximum value to yield an order parameter. The resulting order parameter varies well according to the $(3\cos^2\theta - 1)/2$ expected relationship. Near the magic angle, the sensitivity of the Simplex fitting procedure decreases since the two satellites do not emerge significantly from the central line (see Figure 7). Nevertheless, the perfect matching between the reported order parameter and the expected $(3\cos^2\theta - 1)/2$ relationship is the consequence of a macroscopic ordering of the suspension along a single director. From the deviation detected near the magic angle, we estimate the upper limit of the orientation defects to this macroscopic ordering as 20%, well above the uncertainty introduced by our 5° steps.

IV. Discussion

We reported the occurrence of nematic ordering from a careful analysis of the line shape recorded by ^{23}Na NMR in suspensions of Laponite clay prepared by uniaxial compression. To our knowledge, this is the first direct evidence of macroscopic ordering within dense suspensions of Laponite clays. Previous publications have already reported, from birefringence analysis,^{5,8} such occurrence of nematic ordering within dilute suspensions of Laponite clay, but the observations were not confirmed by direct inspection of the sample after cryofracture.¹¹ It was suggested that this nematic ordering was not an intrinsic property of the clay suspension but was induced by the shear of the suspension during its flow in capillary tubes before the birefringence analysis.

Isotropic/nematic first-order transition of suspensions of anisotropic particles (including disks and cylinders)^{15,16} was predicted by Onsager¹⁴ and observed for a large class of fibrous colloids (Boehmite,^{26–27} Vanadium oxide,^{30–31} tobacco mosaic virus,¹⁵ DNA,^{48–49} polyelectrolytes,² and polymers²⁹) and liquid crystals.^{17–22} The nematic transition was also reported for dilute suspensions (concentration 2%) of platelets (such as Montmorillonite clays²³), but only for particles with an aspect ratio (a = diameter/thickness) much larger than that of Laponite ($a_{\text{Laponite}} = 30$ while $a_{\text{Montmorillonite}} \geq 300$). By contrast, the detection of isotropic/nematic transition of Gibbsite platelets with a low

aspect ratio ($a \sim 11$) required denser suspensions (concentration $\geq 16\%$).²⁵

Because of the slow modulation of the quadrupolar Hamiltonian and the resulting fast relaxation of the satellites, the detection of the quadrupolar splitting of ^{23}Na spectra in dense Laponite suspensions was possible thanks to a fast acquisition procedure, with a dead time of 4.5 μs between the detection pulse and the signal acquisition. Otherwise the central line will only be detected with a loss of 60% of the total magnetization.

The macroscopic ordering of dense Laponite suspensions, detected by ^{23}Na line shape analysis, is the direct proof of the existence of a nematic phase by contrast with a possible birefringent gel.^{5,8} Unfortunately, NMR spectroscopy is not an appropriate tool to distinguish between an equilibrium nematic phase and a nonequilibrium nematic glass.¹⁰ Up to now, no evidence of bulk phase separation is observed, but no complete investigations have been performed in the range of clay concentrations^{3–12} at which this nematic ordering of Laponite suspensions is observed by ^{23}Na NMR. Further studies are now in progress to determine the concentration at which the isotropic/nematic transition occurs by analyzing samples prepared at different pressure. The equation of state of dense suspensions of Laponite will also be measured in these experiments, checking for the occurrence of the first-order isotropic/nematic phase transition. We will also perform structural analysis of these dense clay suspensions by small-angle X-ray scattering in order to check for the periodicity expected in these nematic phases. As an example, for an ordered Laponite sample of 12% vol/vol, this periodicity is expected to be about 100 Å.

Finally, we will also perform numerical simulations of molecular dynamics to calculate the trajectories of sodium cations within the electric field generated by anisotropic charged particles in ordered suspensions and predict their relaxation behavior as we did previously for isotropic dilute suspensions of Laponite clay.

V. Conclusion

^{23}Na nuclear magnetic resonance spectroscopy is used to detect nematic ordering of dense suspensions of Laponite clay by a residual splitting of the sodium resonance line. By contrast with macroscopic ordering, local ordering of dilute Laponite suspensions was already detected by inspection of the variation over a broad range of frequencies of the ^{23}Na nuclear quadrupolar relaxation rates.

Acknowledgment. We cordially thank Drs. R. Setton and S. Rodts (CRMD, Orléans), P. Levitz and D. Petit (PMC, Palaiseau), and F. Fayon (CRMHT, Orléans) for helpful discussions; Dr H. van Damme (ESPCI, Paris) for the gift of the Montmorillonite sample; Drs. D. Massiot and P. Florian (CRMHT, Orléans) for the use of the MSL200 spectrometer. The DSX360 and DSX100 Bruker spectrometers used in this study were purchased thanks to grant from CNRS and Région Centre (France).

Appendix

A. Master Equation. The time evolution of the 3/2 spins is described in the framework of the density operator by the master equation:⁴²

$$\frac{d\sigma^*}{dt} = -i[H_S^*, \sigma^*] + f(\sigma^*) \quad (\text{A1})$$

where H_S^* is the static Hamiltonian including the residual static quadrupolar Hamiltonian and the Hamiltonian describing the radio frequency pulse; $H_{QF}^*(t)$ is the fluctuating component of the quadrupolar Hamiltonian. All calculations are performed in the Larmor frequency rotating frame, as indicated by the asterisk. The second term of eq A1 describes the contribution from the quadrupolar relaxation:

$$f(\sigma^*) = - \int_0^\infty \langle [H_{QF}^*(t), [e^{-iH_S^* \tau} H_{QF}^* + (t - \tau) e^{iH_S^* \tau}, \sigma^*(t)]] \rangle d\tau \quad (\text{A2})$$

The Hamiltonians are developed in a basis set defined by the orthonormal irreducible tensor operators^{42,44-46} T_{lm} ($\text{Tr}\{T_{lm}, T_{l'm'}^+\} = \delta_{ll'} \delta_{mm'}$) for which the Zeeman Hamiltonian is written

$$H_Z = \omega_0 I_Z = \sqrt{5} \omega_0 T_{10} \quad (\text{A3})$$

and the static quadrupolar Hamiltonian becomes

$$H_{QS}^* = \frac{\omega_Q}{6} (3I_Z^2 - I(I+1)) = \omega_Q T_{20} \quad (\text{A4})$$

Furthermore, symmetric and antisymmetric combinations of the operators are introduced

$$T_{lm}(s) = 1/\sqrt{2} (T_{l-m} + T_{lm}) \quad (\text{A5})$$

$$T_{lm}(a) = 1/\sqrt{2} (T_{l-m} - T_{lm})$$

simplifying the notations of the transverse components of the magnetization

$$I_x = \sqrt{5} T_{11}(a); \quad I_y = i\sqrt{5} T_{11}(s) \quad (\text{A6})$$

Finally, the fluctuating component of the quadrupolar Hamiltonian is written:

$$H_{QF}^*(t) = C_Q \sum_{m=-2}^2 (-1)^m T_{2m} e^{im\omega_0 t} (F_{2-m}(t) - \langle F_{2-m}(t) \rangle) \quad (\text{A7})$$

for spin-3/2 nuclei C_Q is $eQ/\sqrt{6}\hbar$ where Q is the quadrupolar moment of the nuclei and $\langle F_{2-m}(t) \rangle$ are the time averaged values of the electric field gradient components F_{2-m} ;

$$F_{20} = V_{zz}, \quad F_{2\pm 1} = \mp \sqrt{\frac{5}{6}} (V_{xz} \pm iV_{yz})$$

and

$$F_{2\pm 2} = \frac{1}{2} (V_{xx} - V_{yy} \pm 2iV_{xy})$$

Equation A1 may be used to calculate the response of the spin system during a RF pulse along the X axis (with angular velocity ω_1). By using eqs A4 and A6, eq A1 becomes

$$\frac{d\sigma^*}{dt} = -i[H_S^*, \sigma^*] + f(\sigma^*) = -i[\omega_Q T_{20} + \sqrt{5} \omega_1 T_{11}(a), \sigma^*] + f(\sigma^*) \quad (\text{A8})$$

By focusing on the secular terms and using eq A7, eq A2 becomes:

$$f(\sigma^*) = -C_Q^2 \sum_{m=-2}^2 \int_0^\infty [T_{2m}, [e^{-iH_S^* \tau} T_{2m} + e^{iH_S^* \tau}, \sigma^*(t)]] \times \langle [F_{2m}^*(t) - \langle F_{2m}^* \rangle] \times [F_{2m}(t - \tau) - \langle F_{2m} \rangle] \rangle e^{im\omega_0 \tau} d\tau \quad (\text{A9})$$

This relaxation contribution introduces in the master equation (cf eq A8) spectral densities at a finite number of frequencies. By neglecting second-order dynamical shifts, we restrict this analysis to the real part of the spectral density

$$J_m(\omega) = 3C_Q^2 \int_0^\infty \langle (F_{2m}^*(t) - \langle F_{2m}^* \rangle) \times (F_{2m}(t - \tau) - \langle F_{2m} \rangle) \rangle \cos(\omega\tau) d\tau \quad (\text{A10})$$

The term ($e^{-iH_s^* \tau} T_{2m} e^{iH_s^* \tau}$) in eq A9 may be developed on the basis of the irreducible tensor operators:

$$e^{-iH_s^* \tau} T_{2m} e^{iH_s^* \tau} = \sum_{p=-2}^2 a_{mp} T_{2p} e^{i\omega_{mp} \tau} \quad (\text{A11})$$

with angular velocities $\omega_{mp} \approx m\omega_0$ for $m \neq 0$. In addition to the classical incoherent contributions to $f(\sigma^*)$, which are proportional to $[T_{2m}, [T_{2m}^+, \sigma^*(t)]]$, coherent contributions proportional to $[T_{2m}, [T_{2p}^+, \sigma^*(t)]]$ must be taken into account. For $m \neq 0$, these contributions to the spectral density oscillate with angular velocities nearly equal to a multiple of ω_0 , because the static quadrupolar Hamiltonian and the irradiating field are much smaller than the Zeeman Hamiltonian. However, these transient components contribute significantly to $f(\sigma^*)$ under the condition⁴¹ $\tau_C \ll (\omega_{mp})^{-1} \ll (|H_{QF}^*|^2 \tau_C)^{-1}$. This condition is not fulfilled in our case for $m \neq 0$, because $\omega_{mp} \approx m\omega_0$, and the decorrelation of the quadrupolar coupling is performed under the slow modulation regime ($\omega_0 \tau_C > 1$) as shown by the frequency variation of the longitudinal relaxation rates (Figure 1). By contrast, eq A11 is explicitly used in this work to treat the time evolution of the $m = 0$ component of $f(\sigma^*)$ as previously described.⁴²

From the previously detailed treatment,⁴² the master equation may be written in a matrix form for the $m \neq 0$ contributions, splitting the whole basis set of the irreducible tensors in two subsets: $\sigma^* = \{T_{11}(a), T_{20}, T_{21}(s), T_{22}(s), T_{31}(a), T_{32}(a), T_{33}(a)\}$ and $\sigma^* = \{T_{10}, T_{11}(s), T_{21}(a), T_{22}(a), T_{30}, T_{31}(s), T_{32}(s), T_{33}(s)\}$:

$$\frac{d}{dt} \begin{pmatrix} T_{11}(a) \\ T_{20} \\ T_{21}(s) \\ T_{22}(s) \\ T_{31}(a) \\ T_{32}(a) \\ T_{33}(a) \end{pmatrix} = \begin{pmatrix} J_1 + 2/5J_2 & 0 & 0 & 0 & -\sqrt{6}/5J_2 & 0 & 0 \\ 0 & 2J_1 + 2J_2 & 0 & 0 & 0 & 0 & 0 \\ 0 & 0 & J_1 + 2J_2 & 0 & 0 & 0 & 0 \\ 0 & 0 & 0 & 2J_1 + J_2 & 0 & 0 & 0 \\ -\sqrt{6}/5J_2 & 0 & 0 & 0 & J_1 + 3/5J_2 & 0 & 0 \\ 0 & 0 & 0 & 0 & 0 & J_2 & 0 \\ 0 & 0 & 0 & 0 & 0 & 0 & J_1 + J_2 \end{pmatrix} \begin{pmatrix} T_{11}(a) \\ T_{20} \\ T_{21}(s) \\ T_{22}(s) \\ T_{31}(a) \\ T_{32}(a) \\ T_{33}(a) \end{pmatrix} \quad (\text{A12})$$

and

$$\frac{d}{dt} \begin{pmatrix} T_{10} \\ T_{11}(s) \\ T_{21}(a) \\ T_{22}(a) \\ T_{30} \\ T_{31}(s) \\ T_{32}(s) \\ T_{33}(s) \end{pmatrix} = \begin{pmatrix} 2/5J_1 + 8/5J_2 & 0 & 0 & 0 & 4/5J_1 - 4/5J_2 & 0 & 0 & 0 \\ 0 & J_1 + 2/5J_2 & 0 & 0 & 0 & -\sqrt{6}/5J_2 & 0 & 0 \\ 0 & 0 & J_1 + 2J_2 & 0 & 0 & 0 & 0 & 0 \\ 0 & 0 & 0 & 2J_1 + J_2 & 0 & 0 & 0 & 0 \\ 4/5J_1 - 4/5J_2 & 0 & 0 & 0 & 8/5J_1 + 2/5J_2 & 0 & 0 & 0 \\ 0 & -\sqrt{6}/5J_2 & 0 & 0 & 0 & J_1 + 3/5J_2 & 0 & 0 \\ 0 & 0 & 0 & 0 & 0 & 0 & J_2 & 0 \\ 0 & 0 & 0 & 0 & 0 & 0 & 0 & J_1 + J_2 \end{pmatrix} \begin{pmatrix} T_{10} \\ T_{11}(s) \\ T_{21}(a) \\ T_{22}(a) \\ T_{30} \\ T_{31}(s) \\ T_{32}(s) \\ T_{33}(s) \end{pmatrix} \quad (\text{A13})$$

where $J_1 = J(\omega_0)$ and $J_2 = (2\omega_0)$.

For $m = 0$, we obtain:

$$\frac{d}{dt} \begin{pmatrix} T_{11}(a) \\ T_{20} \\ T_{21}(s) \\ T_{22}(s) \\ T_{31}(a) \\ T_{32}(a) \\ T_{33}(a) \end{pmatrix} = - \begin{pmatrix} 3/10D & 0 & 0 & -\sqrt{15}/10E & \sqrt{6}/10D & 0 & 0 \\ 3\sqrt{5}/10A & 0 & 0 & \sqrt{3}/2B & \sqrt{30}/10A & 0 & 0 \\ 0 & 0 & 3/2G & 0 & 0 & 3/2F & 0 \\ 3\sqrt{15}/10F & 0 & 0 & 3/2G & 3\sqrt{10}/10F & 0 & 0 \\ 3\sqrt{6}/20I & 0 & 0 & 3\sqrt{10}/20J & 3/10I & 0 & 0 \\ 0 & 0 & 3/2F & 0 & 0 & 3/2G & 0 \\ 3\sqrt{10}/20B & 0 & 0 & \sqrt{6}/4A & \sqrt{15}/10B & 0 & 0 \end{pmatrix} \begin{pmatrix} T_{11}(a) \\ T_{20} \\ T_{21}(s) \\ T_{22}(s) \\ T_{31}(a) \\ T_{32}(a) \\ T_{33}(a) \end{pmatrix} \quad (\text{A14})$$

and

$$\frac{d}{dt} \begin{pmatrix} T_{10} \\ T_{11}(s) \\ T_{21}(a) \\ T_{22}(a) \\ T_{30} \\ T_{31}(s) \\ T_{32}(s) \\ T_{33}(s) \end{pmatrix} = - \begin{pmatrix} 0 & 0 & \sqrt{15}/10A & 0 & 0 & 0 & \sqrt{15}/5B & 0 \\ 0 & 3/10C & 0 & -\sqrt{15}/10A & 0 & \sqrt{6}/10C & 0 & 0 \\ 0 & 0 & 3/2G & 0 & 0 & 0 & 0 & 0 \\ 0 & 0 & 0 & 3/2G & 0 & 0 & 0 & 0 \\ 0 & 0 & \sqrt{15}/5A & 0 & 0 & 0 & -\sqrt{15}/10B & 0 \\ 0 & 3\sqrt{6}/20H & 0 & 3\sqrt{10}/20A & 0 & 3/10H & 0 & 0 \\ 0 & 0 & 0 & 0 & 0 & 0 & 3/2G & 0 \\ 0 & 3\sqrt{10}/20B & 0 & \sqrt{6}/4A & 0 & \sqrt{15}/10B & 0 & 0 \end{pmatrix} \begin{pmatrix} T_{10} \\ T_{11}(s) \\ T_{21}(a) \\ T_{22}(a) \\ T_{30} \\ T_{31}(s) \\ T_{32}(s) \\ T_{33}(s) \end{pmatrix} \quad (\text{A15})$$

where the coefficients A–H are defined in Table 1.

In order to simulate the time evolution of the coherences during each elementary step (RF pulse, time delay or free precession) of the inversion-recovery pulse sequence for the T_1 measurements ($180^\circ x - \tau - 90^\circ x$ -acquisition of I_y) of the Hahn echo pulse sequence for the T_2 measurements ($90^\circ x - \tau/2 - 180^\circ x - \tau/2$ -acquisition of I_y) and the simple pulse for the line shape analysis ($90^\circ x$ -acquisition of I_y), we calculate numerically the eigenvalues and eigenvectors of the matrices obtained by summing the two matrices given in equations A12 and A14 for the first subset of coherences $\{T_{11}(a), T_{20}, T_{21}(s), T_{22}(s), T_{31}(a), T_{32}(a), T_{33}(a)\}$ and in equations A13 and A15 for the second subset of coherences $\{T_{10}, T_{11}(s), T_{21}(a), T_{22}(a), T_{30}, T_{31}(s), T_{32}(s), T_{33}(s)\}$. After the recording of the evolution of $T_{11}(s)$, which is proportional to I_y (cf eq A6), the spectra are evaluated by a fast Fourier transform procedure.

However, the pulse sequence of the $T_{1\rho}$ measurements ($90^\circ x$ -weak irradiation of duration τ along I_y -acquisition of I_y) requires the simulations of the time evolution of the coherences for two different phases of the RF pulse. The master equation governing the time evolution of the coherence during a RF pulse along the y -axis (with angular velocity ω_1) is written as in eq A8:

$$\frac{d\sigma^*}{dt} = -i[H_S^*, \sigma^*] + f(\sigma^*) = -i[\omega_Q T_{20} + i\sqrt{5}\omega_1 T_{11}(s), \sigma^*] + f(\sigma^*) \quad (\text{A16})$$

The same procedure as before⁴² is used to derive the master equation, by treating separately the $m \neq 0$ terms, leading to

$$\frac{d}{dt} \begin{pmatrix} T_{11}(s) \\ T_{20} \\ T_{21}(a) \\ T_{22}(s) \\ T_{31}(s) \\ T_{32}(a) \\ T_{33}(s) \end{pmatrix} = - \begin{pmatrix} J_1 + 2/5J_2 & 0 & 0 & 0 & -\sqrt{6}/5J_2 & 0 & 0 \\ 0 & 2J_1 + 2J_2 & 0 & 0 & 0 & 0 & 0 \\ 0 & 0 & J_1 + 2J_2 & 0 & 0 & 0 & 0 \\ 0 & 0 & 0 & 2J_1 + J_2 & 0 & 0 & 0 \\ -\sqrt{6}/5J_2 & 0 & 0 & 0 & J_1 + 3/5J_2 & 0 & 0 \\ 0 & 0 & 0 & 0 & 0 & J_2 & 0 \\ 0 & 0 & 0 & 0 & 0 & 0 & J_1 + J_2 \end{pmatrix} \begin{pmatrix} T_{11}(s) \\ T_{20} \\ T_{21}(a) \\ T_{22}(s) \\ T_{31}(s) \\ T_{32}(a) \\ T_{33}(s) \end{pmatrix} \quad (\text{A17})$$

and

$$\frac{d}{dt} \begin{pmatrix} T_{10} \\ T_{11}(a) \\ T_{21}(s) \\ T_{22}(a) \\ T_{30} \\ T_{31}(a) \\ T_{32}(s) \\ T_{33}(a) \end{pmatrix} = - \begin{pmatrix} 2/5J_1 + 8/5J_2 & 0 & 0 & 0 & 4/5J_1 - 4/5J_2 & 0 & 0 & 0 \\ 0 & J_1 + 2/5J_2 & 0 & 0 & 0 & -\sqrt{6}/5J_2 & 0 & 0 \\ 0 & 0 & J_1 + 2J_2 & 0 & 0 & 0 & 0 & 0 \\ 0 & 0 & 0 & 2J_1 + J_2 & 0 & 0 & 0 & 0 \\ 4/5J_1 - 4/5J_2 & 0 & 0 & 0 & 8/5J_1 + 2/5J_2 & 0 & 0 & 0 \\ 0 & -\sqrt{6}/5J_2 & 0 & 0 & 0 & J_1 + 3/5J_2 & 0 & 0 \\ 0 & 0 & 0 & 0 & 0 & 0 & J_2 & 0 \\ 0 & 0 & 0 & 0 & 0 & 0 & 0 & J_1 + J_2 \end{pmatrix} \begin{pmatrix} T_{10} \\ T_{11}(a) \\ T_{21}(s) \\ T_{22}(a) \\ T_{30} \\ T_{31}(a) \\ T_{32}(s) \\ T_{33}(a) \end{pmatrix} \quad (\text{A18})$$

from the term $m = 0$, which leads to

$$\frac{d}{dt} \begin{pmatrix} T_{11}(s) \\ T_{20} \\ T_{21}(a) \\ T_{22}(s) \\ T_{31}(s) \\ T_{32}(a) \\ T_{33}(s) \end{pmatrix} = - \begin{pmatrix} 3/10D & 0 & 0 & i\sqrt{15}/10E & \sqrt{6}/10D & 0 & 0 \\ -i3\sqrt{5}/10A & 0 & 0 & -\sqrt{3}/2B & -i\sqrt{3}/10A & 0 & 0 \\ 0 & 0 & 3/2G & 0 & 0 & -i3/2F & 0 \\ i3\sqrt{15}/10F & 0 & 0 & 3/2G & i3/\sqrt{10}F & 0 & 0 \\ 3\sqrt{6}/20I & 0 & 0 & i3\sqrt{10}/20J & 3/10I & 0 & 0 \\ 0 & 0 & i3/2F & 0 & 0 & 3/2G & 0 \\ -3\sqrt{10}/20B & 0 & 0 & i\sqrt{6}/4A & -\sqrt{15}/10B & 0 & 0 \end{pmatrix} \begin{pmatrix} T_{11}(s) \\ T_{20} \\ T_{21}(a) \\ T_{22}(s) \\ T_{31}(s) \\ T_{32}(a) \\ T_{33}(s) \end{pmatrix} \quad (\text{A19})$$

and

$$\frac{d}{dt} \begin{pmatrix} T_{10} \\ T_{11}(a) \\ T_{21}(s) \\ T_{22}(a) \\ T_{30} \\ T_{31}(a) \\ T_{32}(s) \\ T_{33}(a) \end{pmatrix} = - \begin{pmatrix} 0 & 0 & -i\sqrt{15}/10A & 0 & 0 & 0 & -\sqrt{15}/5B & 0 \\ 0 & 3/10C & 0 & i\sqrt{15}/10A & 0 & \sqrt{6}/10C & 0 & 0 \\ 0 & 0 & 3/2G & 0 & 0 & 0 & 0 & 0 \\ 0 & 0 & 0 & 3/2G & 0 & 0 & 0 & 0 \\ 0 & 0 & -i\sqrt{15}/5A & 0 & 0 & 0 & \sqrt{15}/10B & 0 \\ 0 & 3\sqrt{6}/20H & 0 & -i3\sqrt{10}/20A & 0 & 3/10H & 0 & 0 \\ 0 & 0 & 0 & 0 & 0 & 0 & 3/2G & 0 \\ 0 & -3\sqrt{10}/20B & 0 & i\sqrt{6}/4A & 0 & -\sqrt{15}/10B & 0 & 0 \end{pmatrix} \begin{pmatrix} T_{10} \\ T_{11}(a) \\ T_{21}(s) \\ T_{22}(a) \\ T_{30} \\ T_{31}(a) \\ T_{32}(s) \\ T_{33}(a) \end{pmatrix} \quad (\text{A20})$$

References and Notes

- (1) Ottewill, R. H. *Solid/liquid dispersion*; Tadros, Th. F., Ed.; Academic Press: London, 1987; Chapter 9.
- (2) Bonnet-Gonnet, C.; Belloni, J.; Cabane, B. *Langmuir* **1994**, *10*, 4012.
- (3) Ramsay, J. D. F.; Lindner, P. *J. Chem. Soc., Faraday Trans.* **1993**, *89*, 4027.
- (4) Mouchid, A.; Delville, A.; Lambard, J.; Lécolier, E.; Levitz, P. *Langmuir* **1995**, *11*, 1942.
- (5) Gabriel, J. Ch. P.; Sanchez, C.; Davidson, P. *J. Phys. Chem.* **1996**, *100*, 11139.
- (6) Pignon, F.; Magnin, A.; Piau, J. M.; Cabane, B.; Lindner, P.; Diat, O. *Phys. Rev. E* **1997**, *56*, 3281.
- (7) Kroon, M.; Vos, W. L.; Wegdam, G. H. *Phys. Rev. E* **1998**, *57*, 1962.
- (8) Mouchid, A.; Lécolier, E.; Van Damme, H.; Levitz, P. *Langmuir* **1998**, *14*, 4718.
- (9) Saunders, J. M.; Goodwin, J. W.; Richardson, R. M.; Vincent, B. *J. Phys. Chem. B* **1999**, *103*, 9211.
- (10) Bonn, D.; Tanaka, H.; Wegdam, G.; Kellay, H.; Meunier, J. *Europhys. Lett.* **1999**, *45*, 52.
- (11) Levitz, P.; Lécolier, E.; Mouchid, A.; Delville, A.; Lyonard, S. *Europhys. Lett.* **2000**, *49*, 672.
- (12) Nicolai, T.; Cocard, S. *Langmuir* **2000**, *16*, 8189.
- (13) Dijkstra, M.; Hansen, J. P.; Madden, P. *Phys. Rev. E* **1997**, *55*, 3044.
- (14) Onsager, S. *Ann. N.Y. Acad. Sci.* **1949**, *51*, 627.
- (15) Forsyth, P. A.; Marcelja, S.; Mitchell, D. J.; Ninham, B. W. *Adv. Colloid Interface Sci.* **1978**, *9*, 37.
- (16) Eppenga, R.; Frenkel, D. *Mol. Phys.* **1984**, *52*, 1303.
- (17) de Gennes, P. G. *The Physics of Liquid Crystals*; Clarendon: Oxford, 1974.
- (18) Samulski, E. T.; Berendsen, H. J. C. *J. Chem. Phys.* **1972**, *56*, 3920.
- (19) McLachlan, L. A.; Natusch, D. F. S.; Newman, R. H. *J. Magn. Res.* **1973**, *10*, 34.
- (20) Seelig, J.; Niederberger, W. *J. Am. Chem. Soc.* **1974**, *96*, 2069.
- (21) Luz, Z.; Hewitt, R. C.; Meiboom, S. *J. Chem. Phys.* **1974**, *61*, 1758.
- (22) Heinrichsson, U.; Ödberg, L.; Eriksson, J. C. *Mol. Cryst. Liq. Cryst.* **1975**, *30*, 73.
- (23) Langmuir, I. *J. Chem. Phys.* **1938**, *6*, 873.
- (24) Stroobants, A.; Lekkerkerker, H. N. W.; Odijk, Th. *Macromolecules* **1986**, *19*, 2232.
- (25) van der Kooij, F. M.; Lekkerkerker, H. N. W. *J. Phys. Chem. B* **1998**, *102*, 7829.
- (26) Philipse, A. P.; Wierenga, A. M. *Langmuir* **1998**, *14*, 49.
- (27) Wierenga, A.; Philipse, A. P.; Lekkerkerker, H. N. W.; Boger, D. V. *Langmuir* **1998**, *14*, 55.
- (28) Adams, M.; Dogic, Z.; Keller, S. L.; Fraden, S. *Nature* **1998**, *393*, 349.
- (29) Chiccoli, C.; Pasini, P.; Skacej, G.; Zannoni, C.; Zumer, S. *Phys. Rev. E* **1999**, *60*, 4219.
- (30) Pelletier, O.; Sotta, P.; Davidson, P. *J. Phys. Chem. B* **1999**, *103*, 5427.
- (31) Pelletier, O.; Davidson, P.; Bourgaux, C.; Coulon, C.; Regnault, S.; Livage, J. *Langmuir* **2000**, *16*, 5295.
- (32) Porion, P.; Faugère, A. M.; Lécolier, E.; Gherardi, B.; Delville A. *J. Phys. Chem. B* **1998**, *102*, 3477.
- (33) Delville, A.; Porion, P.; Faugère, A. M. *J. Phys. Chem. B* **2000**, *104*, 1546.
- (34) Thompson, D. W.; Butterworth, J. T. *J. Colloid Interface Sci.* **1992**, *151*, 236.
- (35) Ben Ohoud, M.; Van Damme, H. *C. R. Acad. Sci. Paris* **1990**, *311*, 665.
- (36) Deming, S. N.; Morgan, S. L. *Anal. Chem.* **1973**, *45*, 278A.
- (37) Delville, A. *Langmuir* **1991**, *7*, 547.
- (38) Elsass, F.; Beaumont, A.; Pernes, M.; Jaunet, A. M.; Tessier, D. *Can. Mineral.* **1998**, *36*, 1475.
- (39) Kemp-Harper, R.; Brown, S. P.; Hughes, C. E.; Styles, P.; Wimperis, S. *Prog. Nucl. Magn. Reson. Spectrosc.* **1997**, *30*, 157.
- (40) Woessner, D. E.; Bansal, N. *J. Magn. Reson.* **1998**, *133*, 21.
- (41) Petit, D.; Korb, J. P. *Phys. Rev. B* **1988**, *37*, 5761.
- (42) Hancu, I.; van der Maarel, J. R. C.; Boada, F. E. *J. Magn. Reson.* **2000**, *147*, 179.
- (43) van der Maarel, J. R. C.; Jesse, W.; Hancu, I.; Woessner, D. E. *J. Magn. Reson.* **2001**, *151*, 298.
- (44) Jaccard, G.; Pace, R. *Chem. Phys. Lipids* **2000**, *107*, 159.
- (45) Jaccard, G.; Wimperis, S.; Bodenhausen, G. *J. Chem. Phys.* **1986**, *85*, 6282.
- (46) Bowden, G. J.; Hutchison, W. D.; Khachan, J. *J. Magn. Reson.* **1986**, *67*, 415.
- (47) Müller, N.; Bodenhausen, G.; Ernst, R. R. *J. Magn. Reson.* **1987**, *75*, 297.
- (48) Delville, A. *J. Phys. Chem. B* **1999**, *103*, 8296.
- (49) Kassapidou, K.; van der Maarel, J. R. C. *Eur. Phys. J. B.* **1998**, *3*, 471.
- (50) Kassapidou, K.; Jesse, W.; van Dijk, J. A. P. P.; van der Maarel; J. R. C. *Biopolymers* **1998**, *46*, 31.
- (51) Bloembergen, N.; Purcell, E. M.; Pound, R. V. *Phys. Rev.* **1948**, *73*, 679.